



In vitro characterization and *in vivo* ultrasound molecular imaging of nucleolin-targeted microbubbles



Hua Zhang^a, Elizabeth S. Ingham^a, M. Karen J. Gagnon^b, Lisa M. Mahakian^a, Jingfei Liu^a, Josquin L. Foiret^a, Juergen K. Willmann^c, Katherine W. Ferrara^{a,*}

^a Department of Biomedical Engineering, University of California, Davis, CA, 95616, USA

^b Department of Environmental Health and Safety, University of California, Davis, CA, 95616, USA

^c Department of Radiology, Stanford University, Stanford, CA, 94304, USA

ARTICLE INFO

Article history:

Received 18 August 2016

Received in revised form

11 November 2016

Accepted 20 November 2016

Available online 21 November 2016

Keywords:

Angiogenesis

Molecular imaging

Peptide

Ultrasound contrast agents

Nucleolin

In vivo

ABSTRACT

Nucleolin (NCL) plays an important role in tumor vascular development. An increased endothelial expression level of NCL has been related to cancer aggressiveness and prognosis and has been detected clinically in advanced tumors. Here, with a peptide targeted to NCL (F3 peptide), we created an NCL-targeted microbubble (MB) and compared the performance of F3-conjugated MBs with non-targeted (NT) MBs both *in vitro* and *in vivo*. In an *in vitro* study, F3-conjugated MBs bound 433 times more than NT MBs to an NCL-expressing cell line, while pretreating cells with 0.5 mM free F3 peptide reduced the binding of F3-conjugated MBs by 84%, $n = 4$, $p < 0.001$. We then set out to create a method to extract both the tumor wash-in and wash-out kinetics and tumor accumulation following a single injection of targeted MBs. In order to accomplish this, a series of ultrasound frames (a clip) was recorded at the time of injection and subsequent time points. Each pixel within this clip was analyzed for the minimum intensity projection (MinIP) and average intensity projection (AvgIP). We found that the MinIP robustly demonstrates enhanced accumulation of F3-conjugated MBs over the range of tumor diameters evaluated here (2–8 mm), and the difference between the AvgIP and the MinIP quantifies inflow and kinetics. The inflow and clearance were similar for unbound F3-conjugated MBs, control (non-targeted) and scrambled control agents. Targeted agent accumulation was confirmed by a high amplitude pulse and by a two-dimensional Fourier Transform technique. In summary, F3-conjugated MBs provide a new imaging agent for ultrasound molecular imaging of cancer vasculature, and we have validated metrics to assess performance using low mechanical index strategies that have potential for use in human molecular imaging studies.

© 2016 Elsevier Ltd. All rights reserved.

1. Introduction

Although nucleolin (NCL) is primarily known as a nuclear and cytoplasmic protein, NCL is also expressed on the endothelial cell surface, and cell surface-expressed NCL has been identified as an angiogenesis marker [1]. Cell-surface NCL plays a critical role in carcinogenesis [2], and overexpression of NCL is correlated with aggressive tumor progression and poor prognosis [3–5]. Moreover, treatment with a nucleolin antibody can produce endothelial cell apoptosis and normalization of tumor vasculature [6]. In current

clinical practice, the expression level of NCL is tested through biopsy, which is invasive and cannot map the spatial distribution [3–5,7]. Therefore, a non-invasive method to detect and map NCL expression is desired.

As compared with magnetic resonance imaging, x-ray computed tomography and positron emission tomography, ultrasound (US) is attractive for its non-invasiveness, low cost and real-time protocols. US molecular imaging, with targeting moieties conjugated to the surface of microbubbles (MBs), facilitates diagnosis and analysis based on molecular characterization of disease processes, and therefore allows for earlier disease detection [8,9]. Molecular imaging methods also show promise for enhancing diagnostic specificity, guiding therapeutic choices, and monitoring cancer progression and therapeutic response [10–13]. Here, by conjugating an NCL-targeting peptide (F3) to the surface of a MB,

* Corresponding author. Department of Biomedical Engineering, University of California, Davis, 451 Health Sciences Drive, Davis, CA, 95616, USA.

E-mail address: kwferrara@ucdavis.edu (K.W. Ferrara).

we create an NCL-targeted MB (Fig. 1), and evaluate the ability of F3-conjugated MBs to detect NCL expression in the tumor non-invasively.

Compared with other molecularly-targeted constructs or particles, targeted MBs have the following distinguishing characteristics. First, MBs are relatively large contrast agents and often individual voxels contain zero or a few MBs at any time; this is fundamentally different than molecular scale agents (such as small molecules) that are diffusely distributed in other imaging modalities. Therefore, signal processing methods can take advantage of differences in MB concentration as a function of time and space. This is the basis of the projection algorithms explored here. Second, MBs remain in the tumor vasculature due to their micron-scale diameter, enhancing the specificity for imaging tumor vasculature [14,15]. Third, molecularly-targeted MBs clear rapidly from circulation with a blood stream half-life of 3.5 min, with 95% of the MBs cleared from the blood pool after 30 min [16]. Fast clearance of imaging agents ensures practical clinical protocols and enhances the target-to-background ratio. Fourth, the required dose for MB imaging is low with 1×10^{-6} to 1×10^{-4} g administered per kg of body weight (calculated from Refs. [10,17–23]). Fifth, the major components of the MB shell are phospholipids, similar to cell membranes, and therefore immunogenicity is expected to be relatively low [24].

Angiogenesis markers that have been studied in US molecular imaging include $\alpha_v\beta_3$ [10,17], Vascular endothelial growth factor receptor type 2 (VEGFR2) [18–20], B7-H3 (CD276) [21,22], Thymocyte differentiation antigen 1 (Thy1) [25], E-Selectin [26], Endoglin/CD105 [11], Prostate-specific membrane antigen (PSMA) [27], Secreted frizzled related protein-2 [28], and Neuropilin-1 [29]. First-in-human US clinical trials are underway with a molecularly-targeted contrast agent (BR55), where the ligand is targeted to VEGFR2 [8,30]. While the expression of most angiogenesis markers (e.g. $\alpha_v\beta_3$ integrin [17], VEGFR2 [31] and Endoglin [11]) decreases with increasing tumor volume, NCL expression was associated with large tumors (≥ 5 cm) in a cohort of 146 consecutive non-small cell lung cancer patients [4]. Therefore, NCL is an attractive target for non-invasive molecular imaging in advanced cancers (e.g., molecular profiling for NCL expression) and for therapeutic delivery.

NCL targeting ligands, including the oligonucleotide aptamer AS-1411 [32] and the F3 peptide [33], have been used to direct antisense oligonucleotides [34], nanoparticles [35–39], and liposomes [40,41] to tumor blood vessels for imaging [35,36,38,39] and therapeutic applications [34,37–39,41]. AS-1411 is a 29-mer oligonucleotide aptamer (molecular weight (MW) $\sim 14,500$) and F3 is a 34-mer peptide (MW ~ 3500). Based on extensive previous

experience with peptide-conjugated MBs, ease of synthesis and the smaller MW, the F3 peptide was used here to target NCL.

Methods to distinguish the bound-MB signal from that of flowing MBs continue to be developed. Approaches include applying radiation force and imaging protocols to enhance and assess accumulation [42], measuring the signal remaining after the clearance of flowing MBs [30], measuring the signal intensity change caused by a high-intensity US pulse designed to destroy circulating MBs [10,43], averaging images acquired over several seconds to obtain average intensity projections (AvgIPs) [10,43], computing the dwell time [44], and using minimum intensity projections (MinIPs) acquired over several seconds [45].

We have previously shown that high-intensity insonation of targeted MBs can reduce blood flow [43], and therefore our goal is to develop methods to quantify the accumulation and clearance of MB contrast agents using low-intensity US pulse sequences. Given that targeted MBs are now being evaluated in clinical trials and that the use of low transmission intensities is important for widespread clinical use of MBs, the development of such metrics has high significance. While kinetic parameters are also important for breast cancer, as considered here, the diagnosis of liver cancer provides an additional example of the requirement for both accumulation and kinetic parameters. Hepatocellular carcinoma is typically diagnosed by the combination of image hyper-enhancement during the arterial phase and delayed washout in the portal or later contrast phase [46]. Differential diagnosis and the detection of small lesions are expected to be enhanced by targeted contrast agents now in clinical trials [8,14], and the development of metrics for both kinetics and accumulation is important.

Once the projections are created, we have shown previously that a two-dimensional Fast Fourier Transform (2D-FFT) of the projection can differentiate the speckle characteristics associated with bound MBs from the smooth projections associated with flowing MBs [10]. The spectral width of the 2D-FFT peak width increases as MBs bind and can provide a reliable metric for accumulation.

Although most US molecular imaging studies have acquired images in a single plane, 3D US is desirable to map the concentration of agent throughout a tumor [47–49]. Matrix arrays, capable of acquiring 3D data sets, are now available, and therefore 3D protocols are of interest. However, acquiring images from all planes in a volume during the kinetic phase reduces the number of frames available in each slice. Therefore, the impact of the number of acquisition frames on the metrics developed here is also assessed.

2. Materials and methods

2.1. Synthesis of peptides and lipo-peg-peptides (LPPs)

The F3 peptide, F3 LPP and scrambled F3 LPPs were synthesized as in Ref. [50] and described briefly below. The reagents, including solvents, amino acids, Fmoc-Peg27-OH, and Fmoc-Peg4-OH, were obtained from EMD Biosciences (La Jolla, CA) unless otherwise specified. The F3 peptide [1,33], with a sequence of AKVK-DEPQRRSARLSAKPAPPKPEPKPKKAPAKK, and a scrambled F3 peptide (QPAPAPADKDKPKKEKESKSKRKRKRAPAVPPAP) were synthesized in this paper. The syntheses were performed on a Biotage[®] Initiator + Microwave Synthesizer (Biotage, Charlotte, NC), starting with Rink Amide ChemMatrix resin (Biotage, Charlotte, NC) and involved a standard Fmoc protocol [51]. After the two peptides were synthesized on the resin, the peptides were cleaved and the resultant masses were verified with MALDI (Bruker Ultra-Flex extreme MALDI TOF/TOF, Bruker Daltonics Inc., Billerica, MA); both F3 and scrambled peptides had an expected MW of 3729 and measured MW of (H^+) 3731. The two peptidyl resins were then coupled with PEG and lipids on resin manually, as described in

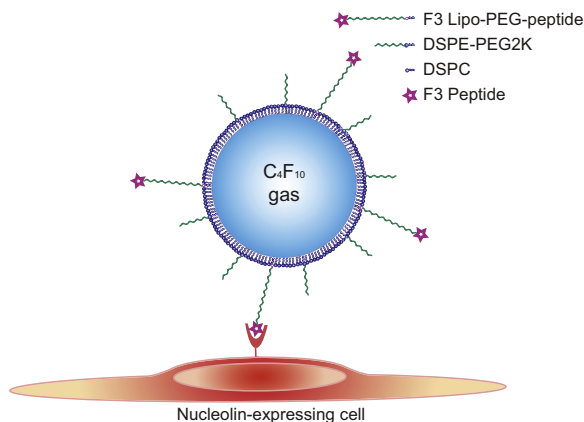


Fig. 1. Schematic of an F3-conjugated MB binding to the surface of an NCL-expressing cell.

Ref. [50]. Starting with the F3 peptidyl resin, the amine group at the N-terminal A₁ was used to couple 3 units of Fmoc-Peg27-OH to create a PEG length of 3564 Da and expose the F3 peptide above the PEG2000 brush layer of the MB surface. For the scrambled F3 LPPs, the amino group on the side chain of K₁₇ of the scrambled F3 peptide was used to couple PEG. Two versions of scrambled F3 LPPs were synthesized: one with a PEG length of 176 Da thus hiding the peptide within the PEG brush (buried scrambled F3, abbreviated as “B-Scr” in this paper) and one with a PEG length of 3564 Da (exposed scrambled F3, abbreviated as “E-Scr” in this paper). After the PEG was coupled onto the peptidyl resin, the Fmoc-Lys(Fmoc)-OH was coupled onto the peptidyl resin. After Fmoc removal, this provided two exposed -NH₂ groups. The two -NH₂ groups were used to couple stearic acid, which anchors the LPP within the lipid layer of the MB surface. The LPPs were then cleaved from the resin and purified with RP-HPLC, and the molecular weights were validated by MALDI (F3 LPP, expected 8301.4 and measured (H⁺) 8302.9; B-Scr LPP, expected 4638.0 and measured (H⁺) 4638.9; E-Scr LPP, expected 8301.4 and measured (H⁺) 8302.9).

2.2. MB preparation

MB components included distearylphosphatidylcholine (DSPC), 1,2-distearoyl-*sn*-glycero-3-phosphoethanolamine-N-[methoxy-(polyethylene glycol)-2000] (ammonium salt) (DSPE-PEG2K) (Avanti Polar Lipids, Alabaster, AL), and LPPs. The non-targeted (NT) MBs have a lipid composition of DSPC:DSPE-PEG2K (90:10 mol/mol), and the targeted MBs have a lipid composition of DSPC:DSPE-PEG2K:LPP = 90:9:1 (molar ratio). MBs were prepared as reported in Ref. [29] and summarized here. First, MB precursors, which are liposome solutions, were made with a thin-film hydration method, and then kept at 4 °C until use. Before use, the liposome solutions were shaken to generate a MB suspension, which was further purified via centrifugation to remove larger and smaller MBs. The size and concentration of the purified MBs were measured with an Accusizer 770A (Particle Sizing Systems, Port Richey, FL), and the MBs were used within 2 h of the final purification.

2.3. Cell culture and MB binding in vitro

An NCL-expressing breast cancer cell line, MDA-MB-435S [33], was purchased from American Type Culture Collection (ATCC, Manassas, VA, # HTB-129). Cells were cultured in Leibovitz's L-15 medium supplemented with 0.01 mg/ml bovine insulin, 0.01 mg/ml glutathione, 10% fetal bovine serum and 1% penicillin–streptomycin. Cells were grown at 37 °C in a humidified air atmosphere incubator and passaged or plated for experiments when 80–90% confluent. For passaging, cells were dissociated from plates using TrypLE™ Express (Invitrogen Corporation, Carlsbad, CA) and split at a subculture ratio of 1:3 to 1:6. For MB binding experiments, 2.5×10^5 cells were seeded onto 25 mm collagen-coated Thermanox™ coverslips (Thermo Fisher Scientific, Waltham, MA) and grown in 35 mm tissue-culture treated dishes for 24 h before use.

F3-conjugated MB binding to MDA-MB-435S was tested and compared with NT MB, following a procedure described in Ref. [29]. Briefly, F3 or NT MB suspensions were applied to plates of MDA-MB-435S cells grown in monolayer at a concentration of 1 or 2×10^7 MB/ml, which was followed with an incubation of 5 min at 37 °C. Free F3 peptide was applied to inhibit MB binding. Coverslips with MDA-MB-435S monolayers were incubated with either phosphate buffered saline (PBS) or F3 peptide in PBS (0.5 mM) at 4 °C for 30 min, prior to the MB treatments (also at 4 °C, with a MB concentration of 0.5×10^7 MB/ml). For each condition, 4 plates of cells were tested (n = 4). Five images were randomly acquired per

plate and analyzed with ImageJ (imagej.nih.gov/ij/), and the MB area per field of view was calculated from the “Analyze Particle” function in ImageJ.

2.4. Tumor model

All animal studies were conducted under a protocol approved by the University of California, Davis Animal Care and Use Committee. Female FVB mice, 5–6 weeks old, 15–25 g, were purchased from Charles River Laboratory International Inc. (Wilmington, MA). Syngeneic breast cancer tumors were grown by transplanting a 1 mm³ piece of donor *neu* exon deletion line (NDL) tumor into each of the bilateral 4th mammary fat pads. Three weeks later, after reaching a maximum diameter of 4–6 mm, the tumors were imaged [52]. Before MB imaging, anesthesia was established with 2% isoflurane (Halocarbon Laboratory, River Edge, NJ) in oxygen (2 L/min), and the animal was placed on a heated stage to maintain body temperature at 37 °C. The hair above and around the tumor was removed by shaving followed by chemical depilatory (Veet, Reckitt Benckiser), and US gel (Aquasonic, Parker Laboratories Fairfield, NJ) was applied to couple the US transducer. MBs were administered by tail vein injection with a 27-gauge needle connected to a cannula. A dose of 2×10^7 MBs in 50 µl saline was injected followed by a 10 µl saline flush.

2.5. Tumor accumulation and specificity

To test *in vivo* performance and specificity, the accumulation of F3-conjugated MBs was compared to that achieved with NT, B-Scr and E-Scr MBs. For each imaging session, MBs were injected consecutively in a random order, and the results from well-perfused tumors were reported here (n = 14, 6, 4, and 6 for F3, NT, B-Scr and E-Scr MBs respectively). The number of consecutive injections per imaging session was limited to 4 or less, to minimize the time under anesthesia and the volume of fluid injected.

2.6. Imaging procedure

US imaging was performed in a manner similar to [10,29], with some modifications (Fig. 2A). MBs were imaged with contrast pulse sequencing (CPS) mode on a Sequoia 512 (Siemens, Issaquah, WA), with a 15L8 transducer. CPS imaging parameters were: a Mechanical Index (MI) of 0.09, a frame rate of 11 Hz and a CPS gain of –12 dB. For each MB injection, a B mode image was acquired before injection to locate the tumor, and CPS clips of 10 s in duration were recorded at the time of injection (0 min), and 0.5, 1, 2, 4, 6, 8, and 8.5 min post injection. A microbubble destruction (MBD) pulse (MI 0.40) was applied at 8.25 min to destroy the MBs. At the 8 min time point, additional MBs did not readily accumulate. Therefore, by comparing images before and after MB destruction, the accumulation of targeted MBs was further validated.

2.7. US image analysis

All of the US images were analyzed offline with MATLAB (Mathworks, Natick, MA) and ImageJ (Fig. 2B). For each of the 10-sec clips, obtained at 0, 0.5, 1, 2, 4, 6, 8 (before MBD), and 8.5 (after MBD) min post injection, motion correction was first performed for each frame, and the AvgIP or MinIP was then obtained.

Motion correction was implemented by minimizing the sum of the absolute difference (SAD) between frames over regions of interest (ROIs). The SAD intensity was then compared with a threshold and frames corresponding to respiration and exceeding this threshold (20% of total frames) were discarded prior to the creation of the projections.

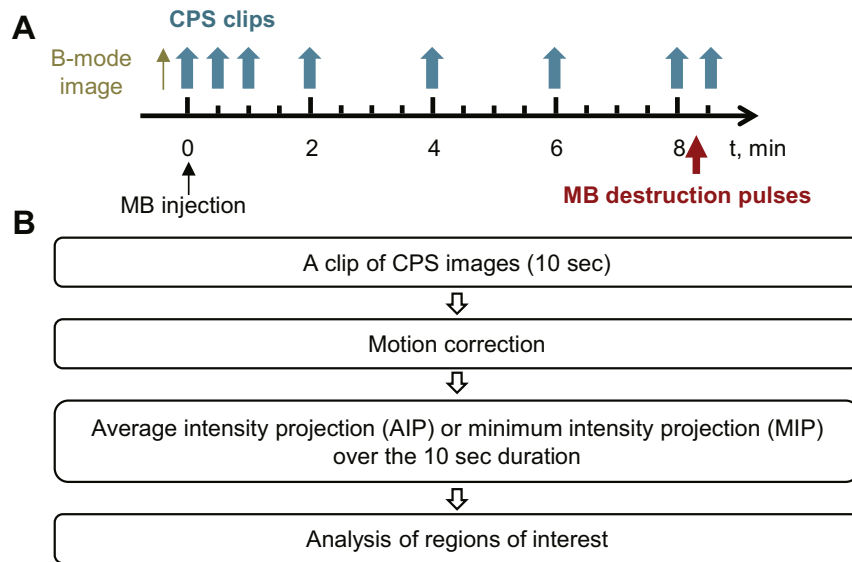


Fig. 2. Schematic showing ultrasound imaging protocol and image quantification procedure. A, one B-mode image was collected before MB injection, ten-second clips of images were acquired in CPS mode at 0, 0.5, 1, 2, 4, 6, 8, and 8.5 min post MB administration, and MB destruction (MBD) pulses were applied at 8.25 min. B, Image clips were processed offline: first, motion correction was performed to remove the effect of physiological motion; second, the average or minimum intensity of each pixel over the 10-sec clip was calculated, resulting in an average intensity projection (AvgIP) or minimum intensity projection (MinIP); third, the AvgIP and MinIP were analyzed within the regions of interest (ROIs).

The concept of the AvgIP and MinIP is summarized in the graphical abstract. For micron-diameter MBs, the AvgIP creates an image that reflects the average US signal in each pixel over 10 s, thus incorporating signals from both bound and flowing MBs. The AvgIP was generated by averaging the aligned CPS frames within the 10-s (110 frames) clip on a pixel-by-pixel basis, as detailed in Ref. [10]. The MinIP estimates the minimum signal in each pixel over 10 s, and is elevated only in regions with bound MBs. The MinIP was generated by finding the minimum intensity for each pixel within the 10-s clip, similar to methods described in Ref. [45]. Quantitative image intensity metrics were then recorded over manually-selected ROIs on the AvgIP or MinIP. For each injection, the tumor intensity readings were normalized by the AvgIP tumor intensity at 30 s post MB injection, which was set as 100, to account for any differences resulting from the injection. The 30-sec time point was chosen to allow for the injected bolus to be mixed throughout the blood volume. The normalized intensities were plotted in time-intensity curves to study kinetics, and used in calculating the intensity difference before and after MB destruction.

2.8. Characterizing bound MBs with the 2D-FFT

The projections were further analyzed with a 2D-FFT to quantify US speckle resulting from bound MBs, with a procedure shown in Supplementary Fig. 2. From an AvgIP or a MinIP, a rectangular area (341×341 pixel², 2×2 cm²) centered on the tumor was processed with the 2D-FFT routine in ImageJ. The resulting 2D-FFT was then converted into a one-dimensional plot of the spectral intensity as a function of the distance from the origin, and the -3 dB spectral width was then calculated.

2.9. Effect of the frame rate and number of frames available to the projections

The effect of frame rate on the projections and the 2D-FFT peak width were studied. The 10-sec CPS image clips were downsampled by 10, 4 or 2 (yielding an effective frame rate of 1.1, 2.75 or 5.5 frames/second, respectively) and the resulting metrics described in

Fig. 2B were compared with those obtained using all data (11 frames/second).

2.10. Statistics

All data are presented as mean \pm standard deviation from 4 or more replicates, calculated in Excel 2010. GraphPad Prism 6.0 was used to generate the multiple comparison statistics in this paper, with either one-way or two-way ANOVA and a multiple comparison correction. Comparisons between two normally-distributed populations were performed using a 2-tailed student *t*-test. A *p* value smaller than 0.05 was considered significant.

3. Results

3.1. Effects of ligand on MB size

Typical size distributions of MBs incorporating 1% F3, B-Scr, or E-Scr LPPs were compared with NT MBs in Fig. 3 and Table 1. Relevant data from MBs with 1% of a smaller peptide (CRPPR) conjugated to a LPP (CRP LPP) [29] are also listed for comparison. Compared with NT MBs, MBs incorporating F3, B-Scr, E-Scr, or CRP LPPs have a similar number-weighted mean diameter (Fig. 3A, C, and Table 1). The volume-weighted mean diameter was greater for MBs incorporating F3, E-Scr, or CRP LPPs ($p < 0.001$, Fig. 3B and C, and Table 1) as compared with NT MBs and MBs incorporating a B-Scr LPP. No significant difference was observed between the volume-weighted diameter of MBs incorporating F3, E-Scr, or CRP LPPs.

3.2. F3-conjugated MB binding to NCL-expressing cells and the inhibition study

Compared with NT MBs, F3-conjugated MBs bound 188 or 433 times more to MDA-MB-435S cells [33], at the concentrations of 1 or 2×10^7 MB/ml, respectively ($p < 0.001$, Fig. 4A–C). Pre-incubating the cells with free F3 peptide (0.5 mM) decreased binding by 84% at 5×10^6 MB/ml ($p < 0.001$, Fig. 4D–F), indicating the specificity of F3-conjugated MB binding.

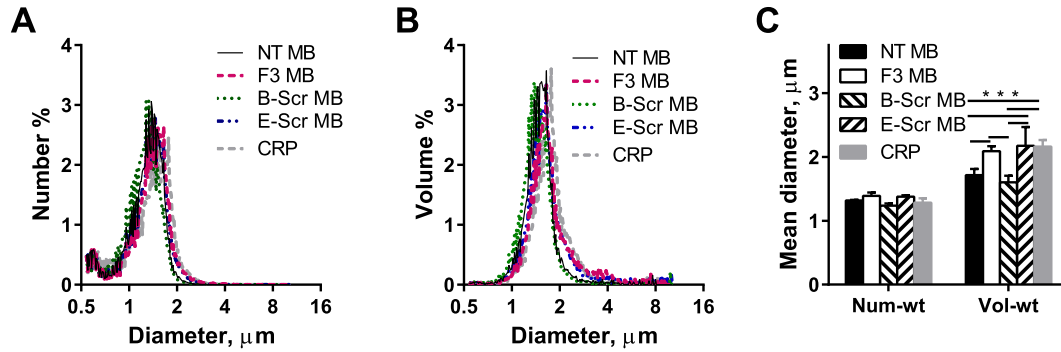


Fig. 3. Size distribution of non-targeted (NT) MBs and MBs including F3, B-Scr, E-Scr or CRPPR (CRP) lipo-PEG-peptides within the shell. A, number-weighted distributions; B, volume-weighted distributions; C, number-weighted and volume-weighted mean diameters, n = 4, two-way ANOVA with Tukey's multiple comparisons test, ***, p < 0.001.

Table 1

MB diameters (μm). # indicates p value from a matched two-way ANOVA resulting in a significant difference in volume-weighted diameter for NT versus F3, E-Scr, and CRP-conjugated MBs and for B-Scr versus F3, E-Scr and CRP-conjugated MBs.

	NT	F3	B-Scr	E-Scr	CRP [29]
Number-weighted	1.32 ± 0.01	1.39 ± 0.05	1.24 ± 0.03	1.38 ± 0.02	1.28 ± 0.07
Volume-weighted	1.72 ± 0.10	2.09 ± 0.09 (p < 0.001) #	1.60 ± 0.10	2.17 ± 0.29 (p < 0.001) #	2.16 ± 0.10 (p < 0.001) #

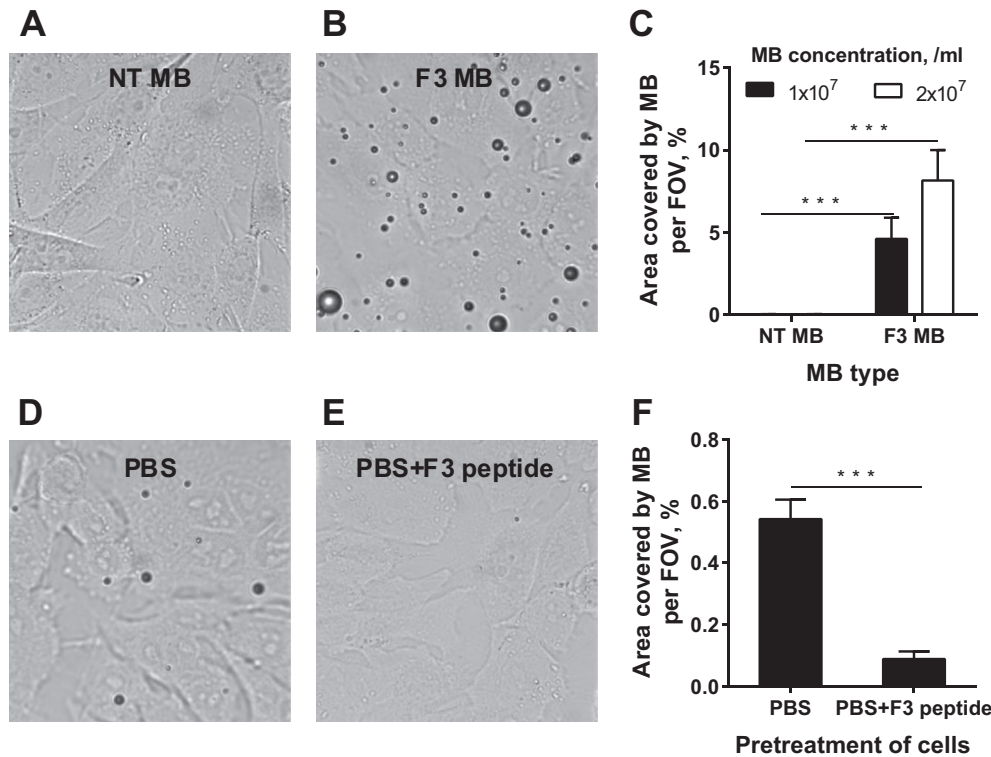


Fig. 4. Comparison of binding of NT and F3-conjugated MBs to an NCL-expressing cell line, and the effect of pretreating the cells with free F3 peptide. Typical images of a cell plate after 5 min incubation at 37 °C with (A) NT MBs or (B) F3-conjugated MBs, at a concentration of 1 × 10⁷ MB/ml. (C) Quantification of area covered by MBs per field of view (FOV). Typical images of F3-conjugated MBs binding to MDA-MB-435S cells at a concentration of 5 × 10⁶ MB/ml after pretreating the cells with (D) PBS or (E) free F3 peptides in PBS (0.5 mM) at 4 °C for 30 min, and (F) the corresponding quantification of area covered by MBs per FOV. Scale bar in A represents 10 μm, n = 4 for each data point. Statistics were determined using a two-way ANOVA with Sidak's multiple comparisons test in C and an unpaired student *t*-test assuming unequal variance in F, ***, p < 0.001.

3.3. *In vivo* MB binding study

Conjugation of the F3 peptide enhanced *in vivo* MB echoes from ND1 tumors (Fig. 5, 1st and 5th rows) more than NT (2nd and 6th rows), B-Scr (3rd and 7th rows), and E-Scr (4th and 8th rows) MBs

in both the AvgIP (upper four rows) and MinIP (lower four rows), with differences particularly evident at later time points, e.g., 8 min.

Based on the tumor AvgIPs, MB echoes increased immediately after injection and reached a maximum at 0.5 min, followed by a decrease from 0.5 to 8 min (Fig. 6A) due to MB clearance from

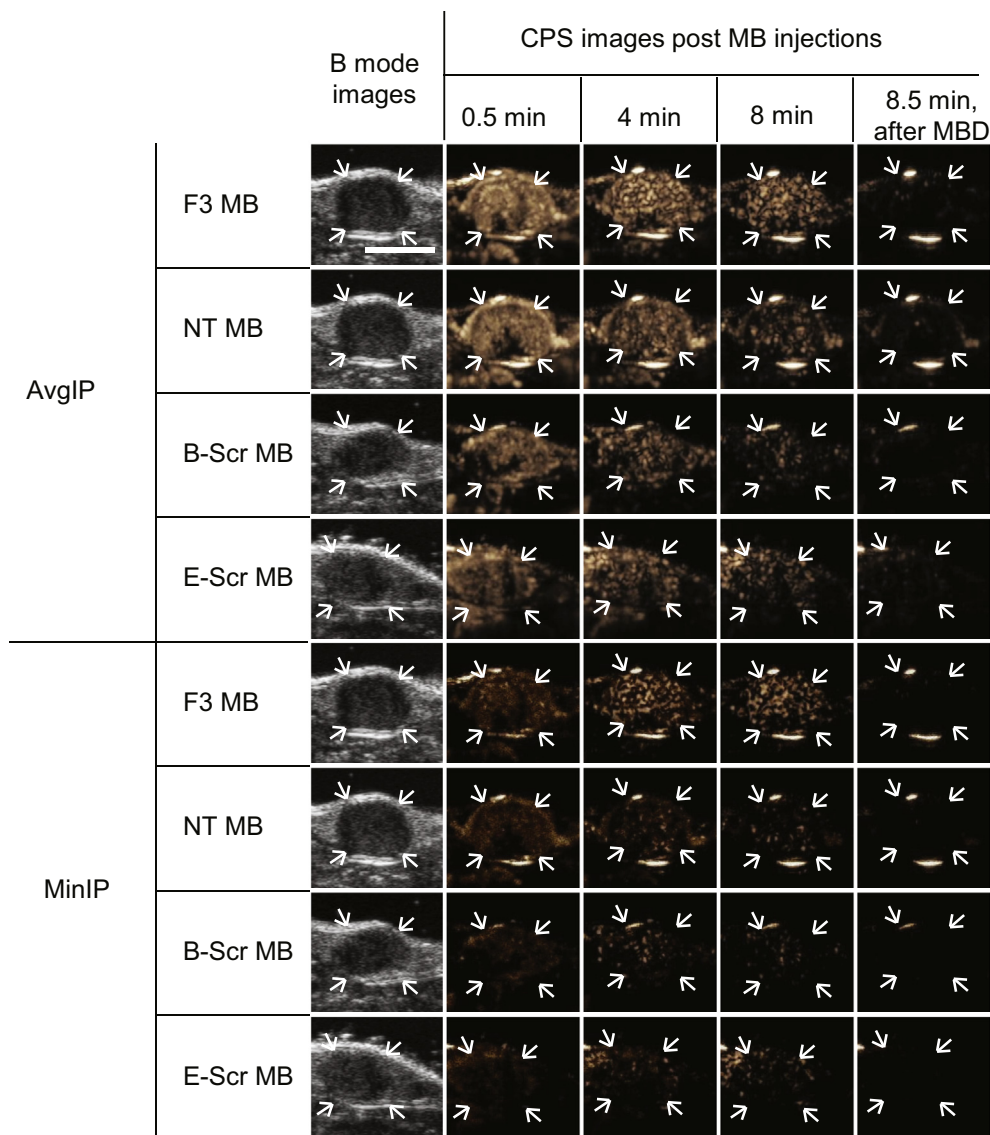


Fig. 5. Typical tumor images after MB administration. B-mode images (first column) are shown for tumor identification, with CPS images (the 4 right columns) acquired at 0.5, 4, 8, and 8.5 min after injection. MB destruction occurred at 8.25 min after injection. The upper/lower four rows are the average or minimum intensity projection images from 10-sec clips, respectively. The scale bar in the top left image represents 5 mm and the white arrows denote the tumor area. Quantification is provided in Fig. 6.

circulation. MBD at 8.25 min further decreased the signal intensity to approximately the intensity observed before injection, indicating most of the signal at 8 min was from bound MBs. Between 0.5 and 8 min after injection, the tumor image intensity from F3-conjugated MBs decreased more slowly than the control MBs, indicating greater accumulation of F3-conjugated MBs. F3-conjugated MB accumulation was greatest for the largest tumors studied and increased with increasing tumor diameter (Supplementary Fig. 1). The signal intensity drop caused by MBD at 8.25 min further validated the targeted accumulation of bound MBs (Fig. 6D, and Table 2).

The MinIPs of the tumors were also quantified to study tumor binding kinetics (Fig. 6B). MB echoes from all formulations increased immediately after injection (0–0.5 min), followed by a slow increase for F3 and E-Scr MBs and a decrease for NT and B-Scr MBs (0.5–8 min), indicating that F3 and E-Scr MBs gradually bound to tumor vasculature while NT and B-Scr MBs did not bind. MBD at 8.25 min after injection decreased the signal intensity to

approximately the level observed before injection (Fig. 6B), again indicating that most of the signal at 8 min was from bound MBs. The signal intensity drop caused by MBD at 8.25 min further characterized the signal intensity from the bound MBs (Fig. 6E, and Table 2).

The difference between the AvgIP and MinIP (Fig. 6C) is proposed as a metric for MB clearance. Here, the kinetics of the vascular clearance was similar for all of the injected agents, as was the goal in the synthesis of these agents.

The 2D-FFT quantified the speckle induced by bound MBs within projections obtained after F3-conjugated MB injection (Fig. 7, Table 3). The AvgIP and MinIP have a similar 2D-FFT spectral width at 0.5 min post injection. The spectral width of both AvgIPs and MinIPs increased with time, indicating that the projections were smooth at early time points due to the presence of the flowing MBs, and speckled at the later time points due to the clearance of flowing MBs and accumulation of bound MBs. The spectrum of the MinIP is wider than that of the AvgIP at later time points as the

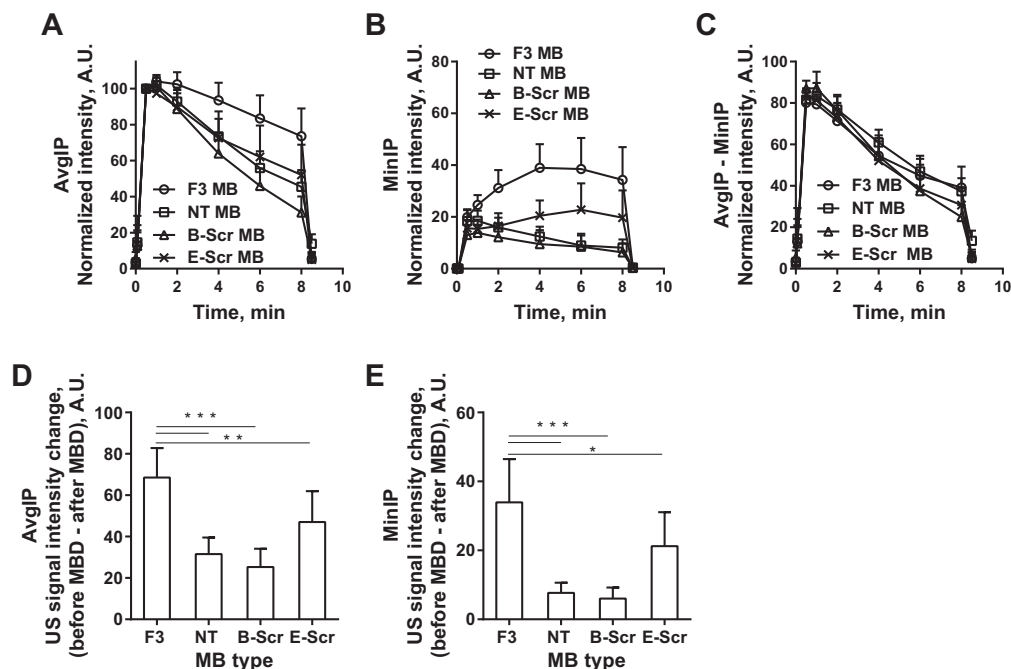


Fig. 6. Time intensity curves for (A) AvgIP, (B) MinIP, and (C) AvgIP–MinIP and the intensity drop caused by MBD for (D) AvgIP and (E) MinIP based on images in Fig. 5. For AvgIPs (A), the MB signal intensity decreased from 0.5 to 8 min. For MinIPs (B), the MB signal intensity increased for F3 and E-Scr MBs, and decreased for NT and B-Scr MBs, from 1 to 8 min. The difference between AvgIP and MinIP depicts the circulating MB signal (C). MBD, applied at 8.25 min, decreased the signal intensity. This decrease was 2.2, 2.7 and 1.5 times greater for F3-conjugated MBs than for NT, B-Scr, and E-Scr MBs, respectively (D). The comparisons were performed with a one-way ANOVA, with Dunnett's multiple comparisons corrections, $n = 14, 6, 4,$ and 6 for F3, NT, B-Scr, and E-Scr MBs, respectively, $*p < 0.05$; $**p < 0.01$; $***p < 0.001$.

Table 2

Signal intensity decrease resulting from MBD. Fold change and p value were obtained from the comparison between F3-conjugated MBs and control MBs with a one-way ANOVA with Dunnett's multiple comparison correction.

	AvgIP				MinIP			
MB type	F3	NT	B-Scr	E-Scr	F3	NT	B-Scr	E-Scr
US intensity drop at MBD	68.1 ± 14.5	31.6 ± 8.0	25.2 ± 8.8	47.0 ± 14.9	33.9 ± 12.5	7.6 ± 3.0	6.0 ± 3.2	21.2 ± 9.9
Fold change	–	2.15	2.69	1.45	–	4.42	5.64	1.60
p value	–	0.0001	0.0001	0.0058	–	0.0001	0.0001	0.039

MinIP suppresses signals from flowing MBs more effectively than the AvgIP. The image intensity for control MBs was low at the later time points and therefore the FFT analysis was not applied to the control agents.

The above image analysis was based on clips with a frame rate of 11 frames/second. In order to assess performance for 3D protocols that usually require lower frame rates, data were downsampled and the performance for reduced frame rates was assessed (Fig. 8 and Table 4). While the AvgIP intensity was not affected by frame rates between 1.1 and 11 frames/second for F3 or NT MBs (data not shown), the MinIP and MinIP intensity reduction at MBD metrics were altered with decreasing frame rate (Fig. 8A–C and Table 4), indicating that a higher frame rate facilitates the elimination of flowing MBs from the MinIP. However, even at the lowest frame rate studied here (1.1 frames/second), the MinIP discriminated bound and flowing MBs, demonstrating the accumulation of F3-conjugated MBs and the clearance of NT MBs (Fig. 8A–B). Further, the ratio between F3 and NT MBs, calculated from the intensity reduction at MBD, was greater for the MinIP than the AvgIP (Table 4).

The 2D-FFT peak width of the MinIP did not change significantly with the frame rate (Fig. 8D), proving the robustness of the peak width in characterizing accumulation. For all of the frame rates

studied in this paper, the peak widths increase similarly with time after injection of F3-conjugated MBs.

4. Discussion

Targeted US contrast agents are useful for preclinical evaluation of vascular receptor expression, and clinical translation is now moving forward. Potential targeting ligands include antibodies [22,53–55], peptides [10,26,30,31,56], or engineered scaffold ligands [57,58]. Methods to conjugate ligands onto the surface of contrast agents have included biotin-avidin coupling [22,43,53–55] and covalent bonds [10,26,30,56,59]. In this paper, a peptide was displayed on the surface of the MB by including a lipo-PEG-peptide during self-assembly. Targeting via a peptide reduces the immune response as compared with an antibody or biotin-avidin interaction.

4.1. F3 peptide as a ligand for MB accumulation

The F3 peptide [60] and F3 peptide-conjugated nanoparticles [35,61] have previously been studied as imaging probes for tumors. F3 peptide-conjugated oligonucleotides [34] and nanoparticles [62] have also been reported as having therapeutic effects in cancer. In

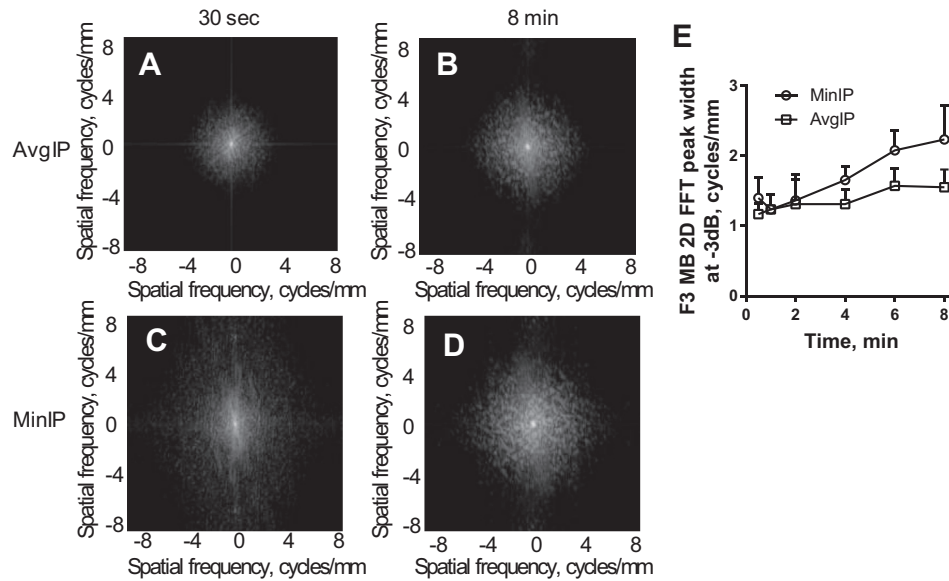


Fig. 7. Typical 2D-FFT spectra of tumor area from (A, B) AvgIPs or (C, D) MinIPs, at (A, C) 30 s or (B, D) 8 min after F3-conjugated MB injection, and (E) the increase of the FFT width (at -3 dB) with time after injection for the AvgIP or MinIP. The FFT peak width increases with time, due to the clearance of the flowing MBs and the retention of bound MBs. The MinIP minimizes the signal from moving MBs and therefore enhances speckle as compared with the AvgIP, resulting in wider 2D-FFT peaks at time points after 4 min. For A–D, the minimum was set as -6 dB of the maximum to enhance visualization.

this paper, F3-conjugated MBs were studied as an imaging probe for tumors and enhanced the tumor image intensity by 4.4 fold more than NT MBs. Further, we found that F3-conjugated MBs accumulate on tumor vasculature over a range of tumor diameters from 2 to 8 mm, supporting the previous finding that tumor vasculature expresses NCL even in advanced disease. Our previous studies targeting MBs to other angiogenic markers have demonstrated a reduced accumulation in advanced disease [29]. Taken together, the results indicate that F3 is an interesting ligand for targeted tumor imaging and for guiding therapy.

With 1% of the ligand in the MB lipid shell, MBs with a buried scrambled F3 peptide (B-Scr MBs) were similar in diameter to NT MBs, while the volume-weighted diameter was greater for F3 and exposed scrambled F3 peptide (E-Scr) MBs. We hypothesize that this effective size difference results from the PEG spacer rather than the peptide properties. This is further supported by the fact that size differences were not observed between F3 and CRPPR MBs, although F3 is a 34-mer with a net charge of $+9$ while CRPPR is a 5-mer with a net charge of $+1$. It has been reported that F3-coated particles bind to NCL-expressing cells and the binding is blocked by free F3 peptide with a concentration of 0.1–1 mM [33,36,63]. This effect was also observed in our MB study. F3-conjugated MBs bound to NCL-expressing cells at a 433 fold greater level than NT MB, and binding was inhibited by pretreating the cells with 0.5 mM free peptide at 4 °C. Interestingly, inhibition was not observed when pre-treatment incubation was performed at 37 °C (data not shown). We hypothesize that this results from the internalizing

properties of the F3 peptide.

The B-Scr LPP was designed to have the same charge but a shorter PEG length as the F3 LPP (176 vs 3564 Da), such that the peptide is buried inside the PEG2000 brush layer on the MB surface. With this structure, B-Scr LPP incorporation did not increase MB binding to tumor vasculature. However, the E-Scr LPP, with the same charge, increased MB binding to $\sim 70\%$ that of F3-conjugated MBs. The F3 peptide is a 34-mer, with 11 unique amino acids, in which Lys, Pro, and Ala are repeated 9, 8, and 6 times, respectively. Further, the scrambled sequence contains elements of the original. Further, with 1% ligand, a one-micron MB has 5×10^4 ligands on the surface [64], and the multivalency effect [65] decreases the affinity difference from two monomeric peptides [50].

4.2. Metrics and image analysis

With the translation of targeted US contrast agents, validation and standardization of quantification methods to separate bound and flowing MB signals are urgently needed. Currently, a widely-used method includes a waiting time (up to 10 min) after injection of targeted MBs to allow for binding to the target site and clearance of flowing MBs from the blood. This is followed by a MB destruction pulse, and the US intensity before and after destruction is recorded and assumed to represent the signal from bound MBs [10]. In this paper, we sought to develop quantitative low mechanical index strategies to detect MB accumulation and assess the kinetics.

The AvgIP magnitude increased with a targeted agent, as compared with a control (NT) agent, but decreased over minutes after injection due to the clearance of the circulating MBs. Most importantly, we found that the MinIP increased as MBs bind to the target vasculature over time. Further, the intensity drop resulting from MBD of MinIPs obtained with F3-conjugated MBs was 4.4 times higher than that obtained with NT MBs, while this measure decreased to 2.2 with AvgIPs (Table 2).

A 2D-FFT of projections was previously used to study the distribution of targeted MBs, with a narrow peak indicating flowing MBs and a wider peak indicating a speckle resulting from bound

Table 3

-3 dB FFT widths (in cycles/mm) for AvgIPs and MinIPs at 30 s or 8 min after MB injection. p value comparisons are indicated by: # for 30 s versus 8 min; ## for AvgIP versus MinIP; ### for 30 s AvgIP versus 8 min MinIP. All are calculated from two-way ANOVA with Tukey correction, $n = 5$.

	30 s	8 min	p
AvgIP	1.17 \pm 0.16	1.55 \pm 0.25	0.292 #
MinIP	1.40 \pm 0.29	2.23 \pm 0.48	0.0004 #
p	0.8853##	0.0047##	<0.0001 ###

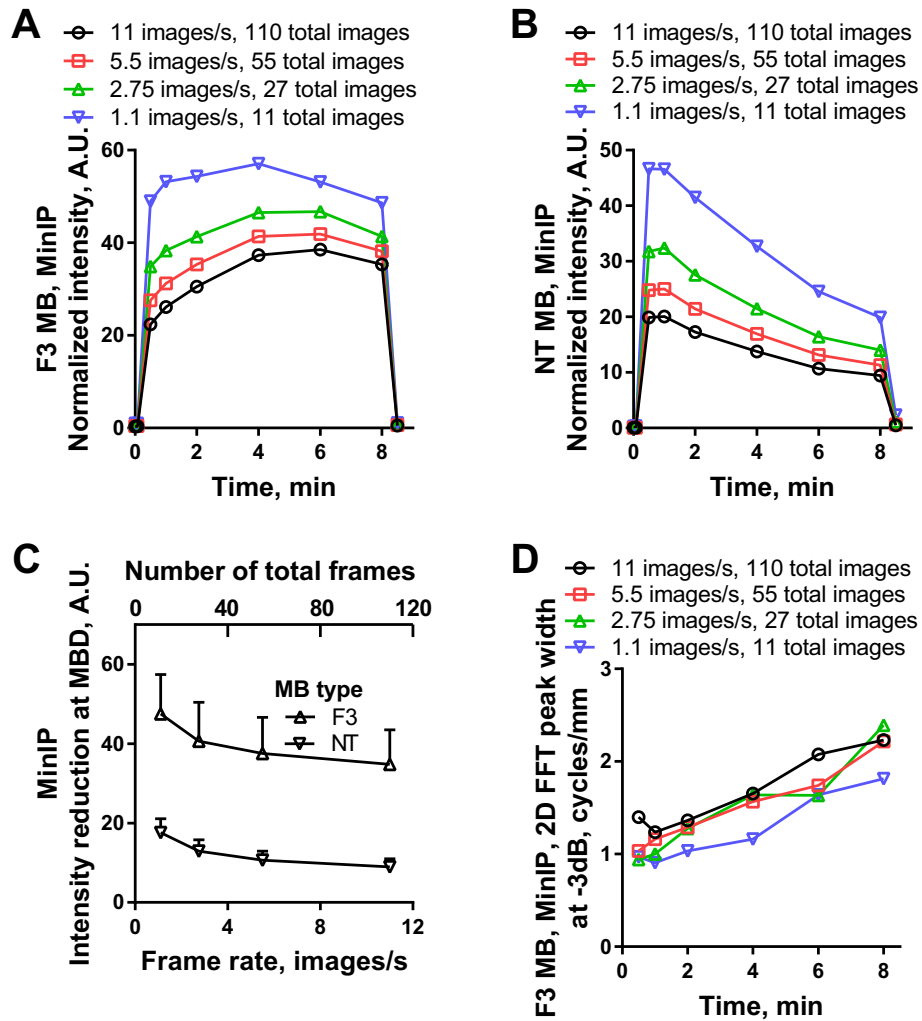


Fig. 8. The effect of frame rate on: (A–B) the mean MinIP for (A) F3 and (B) NT MBs, (C) the intensity reduction at MBD for F3 and NT MBs, and (D) the mean 2D-FFT peak width. With decreasing frame rate, the MinIP intensity increases for both F3 (A) and NT (B) MBs at all time points, indicating a decreasing efficiency in removing the flowing MB signal intensity. The intensity drop at MBD is greater for F3 as compared with NT MBs, and both decrease similarly with frame rate. With increasing time after injection, the 2D-FFT width increases due to increasing speckle and is independent of frame rate.

Table 4
 Effect of frame rate on the signal intensity reduction at MBD.

Frame rate, images/s	11	5.5	2.75	1.1
F3 MinIP	34.8 ± 8.7	37.5 ± 9.1	40.6 ± 9.8	47.5 ± 9.9
NT MinIP	9.0 ± 2.0	10.7 ± 2.3	12.9 ± 2.9	17.6 ± 3.5
F3/NT (MinIP)	3.88	3.52	3.14	2.70
F3/NT (AvgIP)	1.92	1.92	1.92	1.93

MBs [10]. Compared with AvgIPs, the spectrum of MinIPs was broader at 8 min (2.2 ± 0.5 vs 1.6 ± 0.3 cycles/mm, $n = 5$, $p = 0.0047$), indicating that the MinIP minimizes the flowing MB signal more effectively. Such an analysis can complement measures of signal intensity in the quantification of targeted MB accumulation.

The use of the MinIP time-intensity curve to track MB accumulation is attractive as it has the potential to remove the requirement for MBD and the requirement for the injection of a control MB. Although the risks resulting from MBD are relatively small, low mechanical index US protocols have been preferred by contrast agent suppliers during clinical trials, since high-intensity insonation of targeted MBs could potentially induce biological

effects [43]. Similarly, removing the requirement for a control injection would reduce the time required and decrease the already low risk of anaphylaxis. Thus, clinical translation could be greatly simplified.

Tracking the difference between the AvgIP and MinIP over time provides the opportunity to visualize the clearance of MBs from circulation. Here, the rate of (AvgIP–MinIP) decrease for the targeted and control agents was similar, indicating similar wash-out kinetics. Taken together, the data indicate that a single injection of targeted MBs can be used to acquire both the kinetic data for unbound agents and the accumulation of the targeted agent. Therefore, the calculation of both the MinIP and (AvgIP–MinIP) could be useful in many cancers, including breast and liver cancers where both accumulation at the target site and the wash-in and wash-out of NT agents are of interest.

With the development of 3D US molecular imaging, methods to characterize binding with reduced data sets are desirable since volume acquisition reduces the effective acquisition rate to approximately 1 vol per second (and each frame is repeated at this rate). Although the absolute value of the MinIP was altered by decreasing frame rate, the trend in the MinIP over minutes after injection and the 2D-FFT peak width of the projections continued

to provide a robust indication of MB accumulation and clearance.

4.3. Study limitations

The *in vitro* static binding assay used here assesses specificity but does not include the effect of flow conditions. Flow chamber assays provide the opportunity to assess the on/off rates of MB binding and are the subject of ongoing work.

5. Conclusion

In this paper, an F3-conjugated MB was synthesized, and the *in vitro* and *in vivo* performances were compared with NT MBs and scrambled controls. We find that F3-conjugated MBs bind to an NCL-expressing cell line at a level 433 times greater than NT MBs, and this accumulation enhances the detection of syngeneic murine breast tumors. We find that metrics for targeted MB accumulation and metrics for MB wash-in and wash-out can be obtained from the same dose of contrast agent using a low amplitude pulse sequence by calculating the average and minimum intensity projections.

Contributions

Hua Zhang designed and performed experiments, analyzed the experiments results, and drafted the manuscript. Elizabeth S. Ingham performed experiments and contributed to the manuscript. M. Karen J. Gagnon created experimental reagents and contributed to the experimental design. Lisa M. Mahakian performed experiments and contributed to the experimental design. Jingfei Liu and Josquin Foiret analyzed experimental data. Juergen K. Willmann contributed to the experimental design and paper. Katherine W. Ferrara contributed to the experimental design, data analysis and manuscript. All authors have approved the final article.

Acknowledgements

The authors would thank Ms. Sarah Tam for her help in the *in vivo* experiments. Funding: This work was supported by the National Institutes of Health (NIHR01CA112356, NIHR01CA103838, NIHR01CA199658, and NIHR01CA134659).

Appendix A. Supplementary data

Supplementary data related to this article can be found at <http://dx.doi.org/10.1016/j.biomaterials.2016.11.026>.

References

- [1] S. Christian, J. Pilch, M.E. Akerman, K. Porkka, P. Laakkonen, E. Ruoslahti, Nucleolin expressed at the cell surface is a marker of endothelial cells in angiogenic blood vessels, *J. Cell Biol.* 163 (2003) 871–878.
- [2] H. Fujiki, T. Watanabe, M. Suganuma, Cell-surface nucleolin acts as a central mediator for carcinogenic, anti-carcinogenic, and disease-related ligands, *J. Cancer Res. Clin. Oncol.* 140 (2014).
- [3] W. Qiu, F. Zhou, Q. Zhang, X. Sun, X. Shi, Y. Liang, et al., Overexpression of nucleolin and different expression sites both related to the prognosis of gastric cancer, *APMIS* 121 (2013).
- [4] H.Y. Zhao, Y. Huang, C. Xue, Y. Chen, X. Hou, Y. Guo, et al., Prognostic significance of the combined score of endothelial expression of nucleolin and CD31 in surgically resected non-small cell lung cancer, *PLoS One* 8 (2013) 7.
- [5] X. Guo, L. Xiong, L. Yu, R. Li, Z. Wang, B. Ren, et al., Increased level of nucleolin confers to aggressive tumor progression and poor prognosis in patients with hepatocellular carcinoma after hepatectomy, *Diagn. Pathol.* 9 (2014) 1–7.
- [6] V. Fogal, K.N. Sugahara, E. Ruoslahti, S. Christian, Cell surface nucleolin antagonist causes endothelial cell apoptosis and normalization of tumor vasculature, *Angiogenesis* 12 (2009) 91–100.
- [7] L. Peng, J. Liang, H. Wang, X. Song, A. Rashid, H.F. Gomez, et al., High levels of nucleolar expression of nucleolin are associated with better prognosis in patients with stage II pancreatic ductal adenocarcinoma, *Clin. Cancer Res.* 16 (2010).
- [8] L. Abou-Elkacem, S.V. Bachawal, J.K. Willmann, Ultrasound molecular imaging: moving toward clinical translation, *Eur. J. Radiol.* 84 (2015) 1685–1693.
- [9] F. Kiessling, S. Fokong, J. Bzyl, W. Lederle, M. Palmowski, T. Lammers, Recent advances in molecular, multimodal and theranostic ultrasound imaging, *Adv. Drug Deliv. Rev.* 72 (2014) 15–27.
- [10] C.R. Anderson, X.W. Hu, H. Zhang, J. Tlaxca, A.E. Decleves, R. Houghtaling, et al., Ultrasound molecular imaging of tumor angiogenesis with an integrin targeted microbubble contrast agent, *Investig. Radiol.* 46 (2011) 215–224.
- [11] N. Deshpande, Y. Ren, K. Foygel, J. Rosenberg, J.K. Willmann, Tumor angiogenic marker expression levels during tumor growth: longitudinal assessment with molecularly targeted microbubbles and US imaging, *Radiology* 258 (2011) 804–811.
- [12] M.A. Pysz, K. Foygel, J. Rosenberg, S.S. Gambhir, M. Schneider, J.K. Willmann, Antiangiogenic cancer therapy: monitoring with molecular US and a clinically translatable contrast agent (BR55), *Radiology* 256 (2010) 519–527.
- [13] J.H. Zhou, H.J. Wang, H.P. Zhang, A.M. Lutz, L. Tian, D. Hristov, et al., VEGFR2-targeted three-dimensional ultrasound imaging can predict responses to antiangiogenic therapy in preclinical models of colon cancer, *Cancer Res.* 76 (2016) 4081–4089.
- [14] N. Deshpande, A. Needles, J.K. Willmann, Molecular ultrasound imaging: current status and future directions, *Clin. Radiol.* 65 (2010) 567–581.
- [15] J. Fang, H. Nakamura, H. Maeda, The EPR effect: unique features of tumor blood vessels for drug delivery, factors involved, and limitations and augmentation of the effect, *Adv. Drug Deliv. Rev.* 63 (2011) 136–151.
- [16] J.K. Willmann, Z. Cheng, C. Davis, A.M. Lutz, M.L. Schipper, C.H. Nielsen, et al., Targeted microbubbles for imaging tumor angiogenesis: assessment of whole-body biodistribution with dynamic micro-PET in mice, *Radiology* 249 (2008) 212–219.
- [17] Q. Hu, X.Y. Wang, L.K. Kang, H.M. Wei, C.M. Xu, T. Wang, et al., RGD-targeted ultrasound contrast agent for longitudinal assessment of Hep-2 tumor angiogenesis *in vivo*, *PLoS One* 11 (2016).
- [18] M.A. Pysz, S.B. Machtaler, E.S. Seeley, J.J. Lee, T.A. Brentnall, J. Rosenberg, et al., Vascular endothelial growth factor receptor type 2-targeted contrast-enhanced US of pancreatic cancer neovascularity in a genetically engineered mouse model: potential for earlier detection, *Radiology* 274 (2015) 790–799.
- [19] T. Payen, A. Dizeux, C. Baldini, D. Le Guillou-Buffello, M. Lamuraglia, E. Comperat, et al., VEGFR2-targeted contrast-enhanced ultrasound to distinguish between two anti-angiogenic treatments, *Ultrasound Med. Biol.* 41 (2015) 2202–2211.
- [20] S. Wei, N. Fu, Y. Sun, Z. Yang, L. Lei, P. Huang, et al., Targeted contrast-enhanced ultrasound imaging of angiogenesis in an orthotopic mouse tumor model of renal carcinoma, *Ultrasound Med. Biol.* 40 (2014) 1250–1259.
- [21] S.V. Bachawal, K.C. Jensen, K.E. Wilson, L. Tian, A.M. Lutz, J.K. Willmann, Breast cancer detection by B7-H3-targeted ultrasound molecular imaging, *Cancer Res.* 75 (2015) 2501–2509.
- [22] A.M. Lutz, S.V. Bachawal, C.W. Drescher, M.A. Pysz, J.K. Willmann, S.S. Gambhir, Ultrasound molecular imaging in a human CD276 expression-modulated murine ovarian cancer model, *Clin. Cancer Res.* 20 (2014) 1313–1322.
- [23] A.L. Klibanov, Microbubble contrast agents - targeted ultrasound imaging and ultrasound-assisted drug-delivery applications, *Investig. Radiol.* 41 (2006) 354–362.
- [24] A. Elsaesser, C.V. Howard, Toxicology of nanoparticles, *Adv. Drug Deliv. Rev.* 64 (2012) 129–137.
- [25] K. Foygel, H.J. Wang, S. Machtaler, A.M. Lutz, R. Chen, M. Pysz, et al., Detection of pancreatic ductal adenocarcinoma in mice by ultrasound imaging of thymocyte differentiation antigen 1, *Gastroenterology* 145 (2013) 885.
- [26] S. Fokong, A. Fragoso, A. Rix, A. Curaj, Z.J. Wu, W. Lederle, et al., Ultrasound molecular imaging of E-selectin in tumor vessels using poly n-butyl cyanoacrylate microbubbles covalently coupled to a short targeting peptide, *Investig. Radiol.* 48 (2013) 843–850.
- [27] L. Wang, L. Li, Y. Guo, H. Tong, X. Fan, J. Ding, et al., Construction and *in vitro/in vivo* targeting of PSMA-targeted nanoscale microbubbles in prostate cancer, *Prostate* 73 (2013) 1147–1158.
- [28] J.K. Tsuruta, N. Klauber-DeMore, J. Streeter, J. Samples, C. Patterson, R.J. Mumper, et al., Ultrasound molecular imaging of secreted frizzled related protein-2 expression in murine angiosarcoma, *PLoS One* 9 (2014).
- [29] H. Zhang, S. Tam, E.S. Ingham, L.M. Mahakian, C.Y. Lai, S.K. Tumbale, et al., Ultrasound molecular imaging of tumor angiogenesis with a neuropilin-1-targeted microbubble, *Biomaterials* 56 (2015) 104–113.
- [30] S. Pochon, I. Tardy, P. Bussat, T. Bettinger, J. Brochet, M. von Wronski, et al., BR55: a lipopeptide-based VEGFR2-targeted ultrasound contrast agent for molecular imaging of angiogenesis, *Investig. Radiol.* 45 (2010) 89–95.
- [31] J. Bzyl, M. Palmowski, A. Rix, S. Arns, J.M. Hyvelin, S. Pochon, et al., The high angiogenic activity in very early breast cancer enables reliable imaging with VEGFR2-targeted microbubbles (BR55), *Eur. Radiol.* 23 (2013) 468–475.
- [32] F. Mongelard, P. Bouvet, AS-1411, a guanosine-rich oligonucleotide aptamer targeting nucleolin for the potential treatment of cancer, including acute myeloid leukemia, *Curr. Opin. Mol. Ther.* 12 (2010) 107–114.
- [33] K. Porkka, P. Laakkonen, J.A. Hoffman, M. Bernasconi, E. Ruoslahti, A fragment of the HMG2 protein homes to the nuclei of tumor cells and tumor endothelial cells *in vivo*, *Proc. Natl. Acad. Sci. U. S. A.* 99 (2002) 7444–7449.
- [34] E. Henke, J. Perk, J. Vider, P. de Candia, Y. Chin, D.B. Solit, et al., Peptide-conjugated antisense oligonucleotides for targeted inhibition of a

- transcriptional regulator *in vivo*, *Nat. Biotech.* 26 (2008) 91–100.
- [35] G.R. Reddy, M.S. Bhojani, P. McConville, J. Moody, B.A. Moffat, D.E. Hall, et al., Vascular targeted nanoparticles for imaging and treatment of brain tumors, *Clin. Cancer Res.* 12 (2006) 6677–6686.
- [36] M.E. Akerman, W.C.W. Chan, P. Laakkonen, S.N. Bhatia, E. Ruoslahti, Nano-crystal targeting *in vivo*, *Proc. Natl. Acad. Sci. U. S. A.* 99 (2002) 12617–12621.
- [37] Q.Y. Hu, G.Z. Gu, Z.Y. Liu, M.Y. Jiang, T. Kang, D.Y. Miao, et al., F3 peptide-functionalized PEG-PLA nanoparticles co-administrated with tLyp-1 peptide for anti-glioma drug delivery, *Biomaterials* 34 (2013) 1135–1145.
- [38] J.K. Kim, K.J. Choi, M. Lee, M.H. Jo, S. Kim, Molecular imaging of a cancer-targeting theragnostics probe using a nucleolin aptamer- and microRNA-221 molecular beacon-conjugated nanoparticle, *Biomaterials* 33 (2012) 207–217.
- [39] D. Chen, B.W. Li, S.H. Cai, P. Wang, S.W. Peng, Y.Z. Sheng, et al., Dual targeting luminescent gold nanoclusters for tumor imaging and deep tissue therapy, *Biomaterials* 100 (2016) 1–16.
- [40] L.C. Gomes-da-Silva, J.S. Ramalho, M.C.P. de Lima, S. Simoes, J.N. Moreira, Impact of anti-PLK1 siRNA-containing F3-targeted liposomes on the viability of both cancer and endothelial cells, *Eur. J. Pharm. Biopharm.* 85 (2013) 356–364.
- [41] L.Y. Li, J.J. Hou, X.J. Liu, Y.J. Guo, Y. Wu, L.H. Zhang, et al., Nucleolin-targeting liposomes guided by aptamer AS1411 for the delivery of siRNA for the treatment of malignant melanomas, *Biomaterials* 35 (2014) 3840–3850.
- [42] S. Zhao, D.E. Kruse, K.W. Ferrara, P.A. Dayton, Selective imaging of adherent targeted ultrasound contrast agents, *Phys. Med. Biol.* 52 (2007) 2055–2072.
- [43] X.W. Hu, A. Kheirloomoom, L.M. Mahakian, J.R. Beegle, D.E. Kruse, K.S. Lam, et al., Insonation of targeted microbubbles produces regions of reduced blood flow within tumor vasculature, *Investig. Radiol.* 47 (2012) 398–405.
- [44] M.A. Pysz, I. Guracar, L. Tian, J.K. Willmann, Fast microbubble dwell-time based ultrasonic molecular imaging approach for quantification and monitoring of angiogenesis in cancer, *Quant. Imaging Med. Surg.* 2 (2012) 68–80.
- [45] V. Daeichin, Z. Akkus, I. Skachkov, K. Kooiman, A. Needles, J. Sluimer, et al., Quantification of bound microbubbles in ultrasound molecular imaging, *IEEE Trans. Ultrasonics Ferroelectr. Freq. Control* 62 (2015) 1190–1200.
- [46] G.J. Liu, W. Wang, M.D. Lu, X.Y. Xie, H.X. Xu, Z.F. Xu, et al., Contrast-enhanced ultrasound for the characterization of hepatocellular carcinoma and intra-hepatic cholangiocarcinoma, *Liver Cancer* 4 (2015) 241–252.
- [47] J.E. Streeter, R.C. Gessner, J. Tsuruta, S. Feingold, P.A. Dayton, Assessment of molecular imaging of angiogenesis with three-dimensional ultrasonography, *Mol. Imaging* 10 (2011) 460–468.
- [48] H. Wang, O.F. Kaneko, L. Tian, D. Hristov, J.K. Willmann, Three-dimensional ultrasound molecular imaging of angiogenesis in colon cancer using a clinical matrix array ultrasound transducer, *Investig. Radiol.* 50 (2015) 322–329.
- [49] H.J. Wang, D. Hristov, J.L. Qin, L. Tian, J.K. Willmann, Three-dimensional dynamic contrast-enhanced US imaging for early antiangiogenic treatment assessment in a mouse colon cancer model, *Radiology* 277 (2015) 424–434.
- [50] H. Zhang, J. Kusunose, A. Kheirloomoom, J.W. Seo, J.Y. Qi, K.D. Watson, et al., Dynamic imaging of arginine-rich heart-targeted vehicles in a mouse model, *Biomaterials* 29 (2008) 1976–1988.
- [51] W.C. Chan, P.D. White, *Fmoc Solid Phase Peptide Synthesis : a Practical Approach*, Oxford University Press, New York, 2000.
- [52] R.D.H.N. Cardiff, J.A. Engelberg, R.J. Munn, C.H. Miller, J.E. Walls, J.Q. Chen, H.A. Velásquez-García, J.J. Galvez, K.J. Bell, L.A. Beckett, Y.J. Li, A.D. Borowsky, Quantitation of fixative-induced morphologic and antigenic variation in mouse and human breast cancers, *Lab. Invest.* 93 (2013) 480–497.
- [53] J.L. Tlaxca, J.J. Rychak, P.B. Ernst, P.R. Konkalmatt, T.I. Shevchenko, T.T. Pizzaro, et al., Ultrasound-based molecular imaging and specific gene delivery to mesenteric vasculature by endothelial adhesion molecule targeted microbubbles in a mouse model of Crohn's disease, *J. Control. Release* 165 (2013) 216–225.
- [54] J.M. Warram, A.G. Sorace, R. Saini, A.V. Borovjagin, K. Hoyt, K.R. Zinn, Systemic delivery of a breast cancer-detecting adenovirus using targeted microbubbles, *Cancer Gene Ther.* 19 (2012) 545–552.
- [55] E.A. Ferrante, J.E. Pickard, J. Rychak, A. Klibanov, K. Ley, Dual targeting improves microbubble contrast agent adhesion to VCAM-1 and P-selectin under flow, *J. Control. Release* 140 (2009) 100–107.
- [56] C.R. Anderson, J.J. Rychak, M. Backer, J. Backer, K. Ley, A.L. Klibanov, scVEGF microbubble ultrasound contrast agents a novel probe for ultrasound molecular imaging of tumor angiogenesis, *Investig. Radiol.* 45 (2010) 579–585.
- [57] L. Abou-Elkacem, K.E. Wilson, S.M. Johnson, S.M. Chowdhury, S. Bachawal, B.J. Hackel, et al., Ultrasound molecular imaging of the breast cancer neovasculature using engineered fibronectin scaffold ligands: a novel class of targeted contrast ultrasound agent, *Theranostics* 6 (2016) 1740–1752.
- [58] J.K. Willmann, R.H. Kimura, N. Deshpande, A.M. Lutz, J.R. Cochran, S.S. Gambhir, Targeted contrast-enhanced ultrasound imaging of tumor angiogenesis with contrast microbubbles conjugated to integrin-binding knottin peptides, *J. Nucl. Med.* 51 (2010) 433–440.
- [59] J.E. Streeter, P.A. Dayton, An *in vivo* evaluation of the effect of repeated administration and clearance of targeted contrast agents on molecular imaging signal enhancement, *Theranostics* 3 (2013) 93–98.
- [60] M.S. Bhojani, R. Ranga, G.D. Luker, A. Rehemtulla, B.D. Ross, M.E. Van Dort, Synthesis and investigation of a radioiodinated F3 peptide analog as a SPECT tumor imaging radioligand, *PLoS One* 6 (2011) 9.
- [61] J.H. Park, G. von Maltzahn, L.L. Zhang, M.P. Schwartz, E. Ruoslahti, S.N. Bhatia, et al., Magnetic iron oxide nanoworms for tumor targeting and imaging, *Adv. Mater.* 20 (2008) 1630.
- [62] I. Winer, S.Y. Wang, Y.E.K. Lee, W.Z. Fan, Y.S. Gong, D. Burgos-Ojeda, et al., F3-targeted cisplatin-hydrogel nanoparticles as an effective therapeutic that targets both murine and human ovarian tumor endothelial cells *in vivo*, *Cancer Res.* 70 (2010) 8674–8683.
- [63] A.M. Derfus, A.A. Chen, D.H. Min, E. Ruoslahti, S.N. Bhatia, Targeted quantum dot conjugates for siRNA delivery, *Bioconjug. Chem.* 18 (2007) 1391–1396.
- [64] H.I. Petrache, S.W. Dodd, M.F. Brown, Area per lipid and acyl length distributions in fluid phosphatidylcholines determined by ²H NMR spectroscopy, *Biophys. J.* 79 (2000) 3172–3192.
- [65] D. Peer, J.M. Karp, S. Hong, O.C. Farokhzad, R. Margalit, R. Langer, Nanocarriers as an emerging platform for cancer therapy, *Nat. Nano* 2 (2007) 751–760.